Molecular Basis of Mesophase Ordering in a Thiophene-Based Copolymer

Dean M. DeLongchamp,*,† R. Joseph Kline,† Youngsuk Jung,† Eric K. Lin,† Daniel A. Fischer,† David J. Gundlach,† Sarah K. Cotts,† Andrew J. Moad,† Lee J. Richter,† Michael F. Toney,‡ Martin Heeney,§ and Iain McCulloch||

National Institute of Standards and Technology, Gaithersburg, Maryland 20899; Stanford Synchrotron Radiation Laboratory, Menlo Park, California 94025; Department of Materials, Queen Mary, University of London, London E1 4NS, U.K.; and Department of Chemistry, Imperial College of London, London SW7 2AZ, U.K.

Received February 27, 2008; Revised Manuscript Received April 23, 2008

ABSTRACT: The carrier mobility of poly(2,5-bis(3-alkylthiophen-2-yl)thieno[3,2-*b*]thiophene) semiconductors can be substantially enhanced after heating through a thermotropic mesophase transition, which causes a significant improvement in thin film structural order. By directly measuring film structure throughout a heating and cooling cycle, we identify the molecular origin of this mesophase transition as the melting of interdigitated linear alkane side chains, in this case quaterdecyl. The morphology and phase behavior throughout the thermal cycle are controlled by the changing conformation of the side chains. Surprisingly, the melting of the side chains allows increases in the backbone order, $\pi-\pi$ stacking, and carrier mobility. Upon cooling, the side chains recrystallize to preserve the excellent mesophase order and enhanced electrical performance.

Introduction

Organic semiconductors are promising active layers for low-cost and flexible electronics that can be deposited by additive processes such as printing.[1,2] An important consequence of solution deposition is that the semiconductor microstructure forms dynamically upon solidification. The low molecular diffusivity of polymer semiconductors during solidification typically results in poor packing and nonequilibrium microstructures,[3] often yielding domains less than ≈20 nm with many boundaries where π overlap is poor.[4] Polymer semiconductor films therefore typically exhibit lower carrier mobility than highly crystalline films of vapor-deposited small molecules such as pentacene,[5] which have greater diffusivity during solidification, facilitating assembly into large, micrometer-scale domains.

A promising approach to improve the order of solution-deposited polymer films has recently been demonstrated with the development of polymers[6–8] that exhibit a thermotropic mesophase transition. Heating films of these new polymers above this mesophase transition results in the growth of relatively large, highly ordered domains. Carrier mobility after a thermal cycle through the mesophase rivals that of vapor-deposited small molecules and even amorphous silicon.[7] This transition is not observed[3] in earlier semiconducting polymers such as regioregular poly(3-hexylthiophene) (rr-P3HT).[9] Microstructure measurements of films before and after mesophase heating have revealed dramatic improvements in film order,[6–8] yet the molecular origins of this mesophase transition and its relationship to the development of order have not been established.

In this report we determine the molecular origin of the three-dimensional order that develops when one of these high carrier mobility polymers, poly(2,5-bis(3-quaterdecylthiophene-2-yl)-thieno[3,2-*b*]thiophene) (pBTTT, Figure 1), is heated to its mesophase. Microstructure development throughout a heating cycle is characterized in situ by specular X-ray diffraction (XRD) to follow changes in the film order perpendicular to the substrate, while a combination of in situ polarized absorption spectroscopies (infrared, visible, and X-ray) are applied to determine changes in the conformations and orientations of the side chains and conjugated backbone. This combined approach allows characterization of virtually all aspects of film structure as they change with temperature.

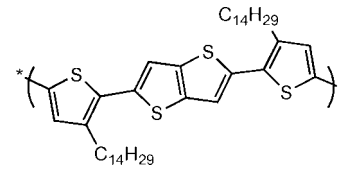

Figure 1. Primary chemical structure of pBTTT.

Materials and Methods

pBTTT was synthesized by previously described methods.[7] Differential scanning calorimetry (DSC) measurements were performed on pBTTT powder using a TA-Q1000[36] with a heating and cooling rate of 10 °C/min. Silicon substrates were hydrophobically modified by cleaning in an ultraviolet ozone cleaner for 10 min, rinsing with deionized water, and immersing in a 0.002 mol/L hexadecane solution of octadecyltrichlorosilane (OTS8) at room temperature for 16 h. Substrates were then cleaned in a Bransonic ultrasonic cleaner for 15 min in chloroform, isopropanol, and deionized water and heated atop a hot plate to 150 °C for 10 min. Hydrophobic substrate modification was confirmed by a water contact angle of 105°−107°. pBTTT was dissolved at 3.5 mg/mL in a mixture of 8:1 by volume chloroform to dichlorobenzene. Films were spin-cast from 80 °C solution at 3000 rpm with fast acceleration. Typical film thickness by spectroscopic ellipsometry (SE) measurement was ≈25 nm. All pBTTT formulation and processing were performed in a nitrogen environment.

Specular XRD was performed on a modified commercial diffractometer with a Cu Kα source. Samples were kept under vacuum in a beryllium-windowed chamber atop a heated copper block. Typical collection time for specular XRD was ≈30 min per temperature. Grazing incidence X-ray diffraction (GIXD) was performed at the Stanford Synchrotron Radiation Laboratory on

* Corresponding author. E-mail: deand@nist.gov.
† National Institute of Standards and Technology.
‡ Stanford Synchrotron Radiation Laboratory.
§ Queen Mary, University of London.
|| Imperial College of London.

10.1021/ma800440f CCC: $40.75
Published on Web 07/01/2008

beamline 7-2; the films were illuminated with an 8 keV beam at a constant incidence angle of ≈0.2°. Samples were kept under flowing helium in the poly(ethyl ether ketone) dome of an Anton-Parr temperature chamber. The diffracted beam resolution was set by 1 mrad Soller slits. To account for thermal drift, the sample was realigned at each temperature.

Near-edge X-ray absorption fine structure (NEXAFS) spectroscopy was performed at National Institute of Standards and Technology beamline U7A of the National Synchrotron Light Source. Carbon K-edge collection was performed in partial electron yield mode with a grid bias of −50 V. Spectra were collected at five incident angles and normalized with respect to carbon concentration by their intensity at 330 eV. NEXAFS carbon K-edge measurements were performed by necessity a high-vacuum environment. Typical soak/collection time for NEXAFS was ≈20 min per temperature.

SE was collected at three angles from the surface plane (45°, 30°, and 15°) with an M 2000 series ellipsometer (J.A. Woollam Co., Inc.) and analyzed using vendor supplied software. To reduce correlations in the extracted uniaxial dielectric functions, measurements were made on identical films on two substrates: Si wafers terminated with an OTS8-modified native oxide or 200 nm thick thermal oxide. Typical soak/collection time for SE was ≈17 min per temperature for the sample pair.

Polarized, Transmission Fourier Transform IR. Fourier transform IR (FTIR) spectroscopy was performed using a Magna 860 FTIR (Thermo Nicolet) on films cast on double side polished Si substrates with the sample tilted at Brewster's angle of 16.3° with respect to the incident beam. Polarization was controlled via a wire grid polarizer. Typical soak/collection time for FTIR was ≈14 min per temperature. Samples were kept under nitrogen for both SE and FTIR measurements.

Organic field effect transistors (FETs) were prepared by spin-coating pBTTT onto bottom gate, bottom contact test structures with an OTS-modified, 230 nm thick thermally grown silicon oxide gate dielectric and a common gate of highly doped silicon. Source and drain contacts were afforded by an interdigitated gold electrode array of channel length of 20 μm and channel width of 1 cm fabricated by lift-off photolithography. Devices were probed in a nitrogen-purged Cascade probe station; electrical measurements were performed with two Keithley 6430 and one Keithley 2100 with a common floating ground. Field-effect hole mobilities were extracted in the saturation regime from the linear fit of the square root of source-drain current vs gate potential. A typical soak/collection time for FET measurement was ≈10 min per temperature.

Results and Discussion

The temperature of the mesophase transition in pBTTT powder was determined by differential scanning calorimetry (DSC), shown in Figure 2, which reveals two transitions during the first heating ramp. A lower temperature transition is observed at $T_{H1} \approx 60$ °C, and a higher transition is observed at $T_{H2} \approx 158$ °C. Upon cooling, only a single transition is observed at $T_C \approx 100$ °C. No lower temperature cooling transition analogous to the T_{H1} transition is observed down to −50 °C. Over the second heating cycle, the T_{H1} transition is not observed, and the T_{H2} transition occurs at a slightly lower temperature (148 °C) and with greater heat flow. The T_C transition of the second cycle is identical with the first.

The observation of two heating endotherms but only a single cooling exotherm suggests that the powder contains some pBTTT that is not in the thermodynamic equilibrium state but is instead at a local free energy minimum, described as a transient or metastable state. This state is eliminated by heating above T_{H2} and recrystallizing through T_C. The sharp definition of the T_{H1} endotherm suggests that the microstructure of the metastable state is well-defined rather than disordered. The change in position and magnitude of the T_{H2} transition in the second cycle suggests that pBTTT in the metastable phase for the first cycle contributes to the T_{H2} transition in the second cycle. A higher temperature phase change, not shown here but reported previously,[7] occurs at ≈233 °C.

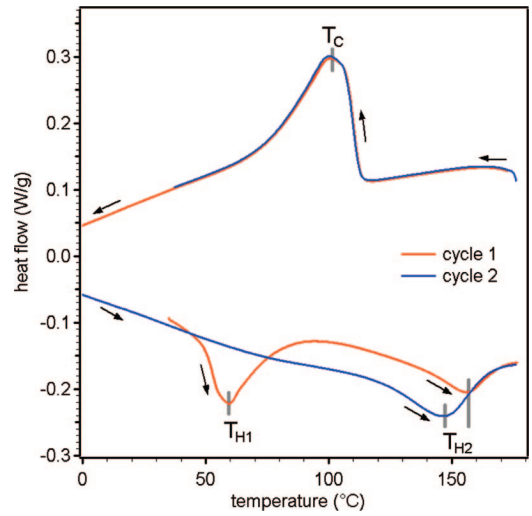

Figure 2. Differential scanning calorimetry of pBTTT powder. Experimental standard uncertainty is less than 1%.

Thin pBTTT films, after they are heated above T_{H2} and recrystallized through T_C (a process we will hereafter call annealing), exhibit a layered microstructure of slightly tilted, π-stacked conjugated backbones. The microstructure of pBTTT becomes substantially more aligned and ordered upon annealing, and the carrier mobility increases.[7] Annealed pBTTT films exhibit exceptional levels of backbone positional order in the layer stacking and π stacking directions compared to rr-P3HT of similar molecular mass.[7] The alkane side chains of pBTTT are substantially tilted from the surface normal and significantly interdigitated between layers.[10] The density of the interdigitated pBTTT side chains in their closest-packed plane is nearly that of crystalline polyethylene, and their methylene groups exhibit few gauche defects. It is suggested that interdigitation of the side chains promotes three-dimensional ordering and is a key advantage of polymers such as pBTTT over earlier, lower-performance semiconducting polymers such as rr-P3HT.[11]

The molecular origin of the pBTTT mesophase transition is suspected to relate to the side-chain conformation because T_{H2} shifts with changing alkane side-chain length, whereas the temperature of the higher temperature transition remains constant near 233 °C. The packing of the conjugated backbone contributes strongly to the energetic stability of the pBTTT crystal,[10] so it is reasonable to expect that the phase transition near 233 °C may result from the disordering of backbone packing.

We have characterized the T_H/T_C mesophase transition in pBTTT films ≈25 nm thick prepared by spin-coating atop octyltrichlorosilane (OTS8)-treated silicon oxide. We focus primarily on first heating and cooling cycles to examine the technologically important mechanism of microstructure and mobility improvement by annealing. We consider second cycle data for certain measurements to highlight the molecular nature of the mesophase. The temperature of a mesophase change can be sensitive to the rate of temperature change, which for this study varies depending on the requirements of the analytical technique used. Even with significant differences in measurement times among techniques, T_H and T_C agree reasonably well with the DSC transition temperatures when they are detected by relevant structure measurements as described below.

The layered microstructure of pBTTT films results in a series of (h00) diffraction peaks in specular XRD (Figure S1). The (200) Bragg peak is the most straightforward to analyze because it is intense but unaffected by the reflectivity background. Specular XRD of the (200) peak was collected while an as-cast

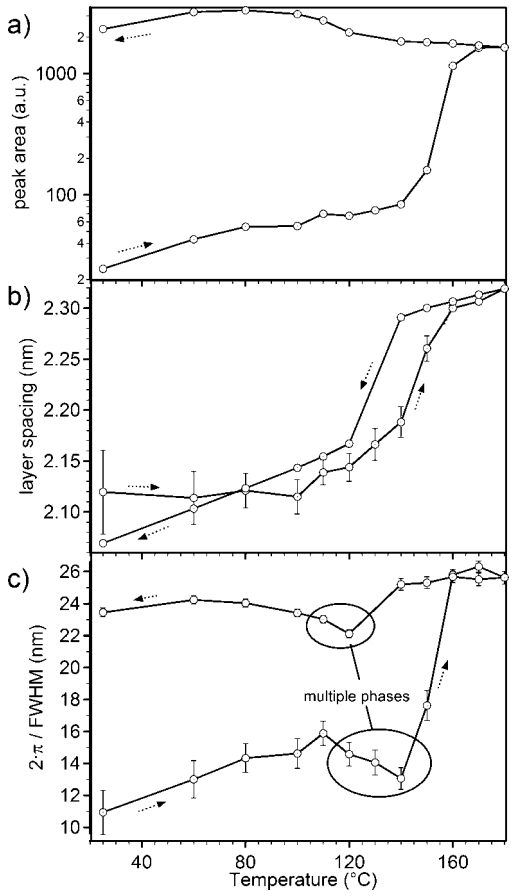

Figure 3. pBTTT lamellar order from analysis of the (200) peak in thin film specular XRD for first cycle heating: (a) overall peak area (integrated intensity), note logarithmic scale; (b) layer spacing; (c) approximate domain size along surface normal from the Scherrer relationship. Arrows indicate the development of these quantities through the first heating cycle. Lines are to guide the eye. Error bars represent the uncertainty of fit; in (a) error bars are less than the marker thickness. Raw XRD data are provided in the Supporting Information.

pBTTT film was heated to 180 °C and then cooled. Analysis of the (200) diffraction peak provides the extent of layer order/alignment, the layer spacing within domains, and the approximate thickness of well-ordered domains.

Both greater layer order and better layer alignment parallel to the substrate plane increase the (200) Bragg peak area. Changes in peak area over a heating cycle are shown in Figure 3a. The peak area modestly increases by a factor of ≈3.0 upon heating from 25 to 100 °C. This temperature range corresponds to the T_{H1} transition, so the melting of the transient phase may be responsible for the increased order and/or alignment. The peak area increases by a much larger factor of ≈20 from 140 to 170 °C, across the T_{H2} transition and into the mesophase. The relatively constant peak area above 160 °C indicates that the layer structure no longer changes substantially within the mesophase. Upon cooling, the peak area remains constant to ≈120 °C, where it begins to further increase, consistent with T_C from DSC. The peak area thereafter appears relatively stable at temperatures lower than 100 °C.

Changes in the vertical layer spacing over a heating cycle, determined from the position of the (200) Bragg peak center, are shown in Figure 3b. The layer spacing does not increase significantly when heating from 25 to 100 °C. The pBTTT crystal should exhibit thermal lattice expansion, but the measured layer spacing also includes contributions from the metastable state, which could have a different layer spacing and furthermore melts across this temperature range, as shown by the DSC data. After the metastable state is completely melted, we observe a nearly linear increase in layer spacing from 100 to 140 °C. The layer spacing expands abruptly to 2.30 nm over the T_{H2} transition and then once again exhibits a linear increase once within the mesophase. The recrystallization contraction occurs at ≈120 °C. The cooling trend reveals linear dependences of layer spacing on temperature within each phase and in particular shows the expected thermal dependence of the pBTTT lattice that was obscured during heating.

A final quantity that can be extracted from specular XRD is the approximate domain size normal to the substrate. If one assumes that the Scherrer relationship[12] is valid, the domain size along the surface normal (the "domain thickness") can be related to the full width at half-maximum of a Bragg peak.[13] The development of domain thickness with temperature is shown in Figure 3c. Domain thickness is ≈12 nm as cast and increases modestly to ≈16 nm as temperature increases to 100 °C. Domain thickness appears to decrease approaching 140 °C, and then it increases abruptly from 140 to 160 °C, where it achieves a plateau of ≈26 nm, which is the approximate total film thickness. Upon cooling, the domain thickness remains near the film thickness. The small dips in domain thickness that appear near the T_{H2} phase transition while heating and cooling are most likely due to broadening of the Bragg peak by the coexistence of crystalline and mesophase components with different layer spacings and therefore may not accurately reflect the domain thicknesses at those temperatures. For the same reason, it is likely that contributions from the metastable state and its melt decrease the apparent domain thickness during the heating ramp at temperatures below T_{H2}.

We note that in some cases rr-P3HT can exhibit a small increase in crystallinity with film heating to 150 to 180 °C.[3,14–17] This increase may be analogous to the modest increase we observe in pBTTT (200) peak area from 25 to 140 °C. It has been reported that heating in this temperature range can improve the field effect mobility of some rr-P3HT films,[14] but not others.[15–17] Importantly, equilibrium phase changes do not appear to be responsible for these modest improvements in P3HT microstructure. It is possible that the melting of a metastable state is instead responsible. Microstructure improvements of the magnitude caused by the pBTTT T_{H2} mesophase transition have not been observed in P3HT for heat treatments below its sole consistently reported phase transition, a ≈240 °C backbone melt that is analogous to the ≈233 °C phase transition of pBTTT.

The development of in-plane order in pBTTT films over its mesophase transition can be further examined with GIXD, which reveals in-plane positional order. GIXD results are shown in Figure 4. Two significant peaks are observed: the (003), corresponding to regular order along the pBTTT backbone, and the (010), corresponding to regular order between backbones. The location of the (003) corresponds to a spacing of ≈1.34 nm, which is approximately the pBTTT repeat unit length. At room temperature, the $\pi-\pi$ interplane backbone spacing taken from the location of the (010) peak is ≈0.370 nm. At 180 °C, both peaks remain. The spacing between backbones expands to ≈0.381 nm, while the (003) peak does not shift position. The $\pi-\pi$ stacking of pBTTT therefore persists above the mesophase transition T_{H2}.

Surprisingly, the XRD measurements clearly show that the exceptional vertical layer order of pBTTT is established upon entering the mesophase through T_{H2}, not upon recrystallization to the room temperature phase through T_C. Heating to the mesophase apparently provides molecular mobility sufficient to grow highly ordered domains of a single phase to the full film thickness. When the film cools, this high level of layer order is

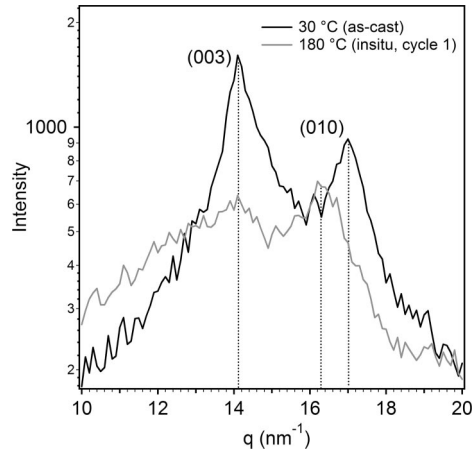

Figure 4. GIXD patterns of a pBTTT film as cast and then when heated in situ to 180 °C.

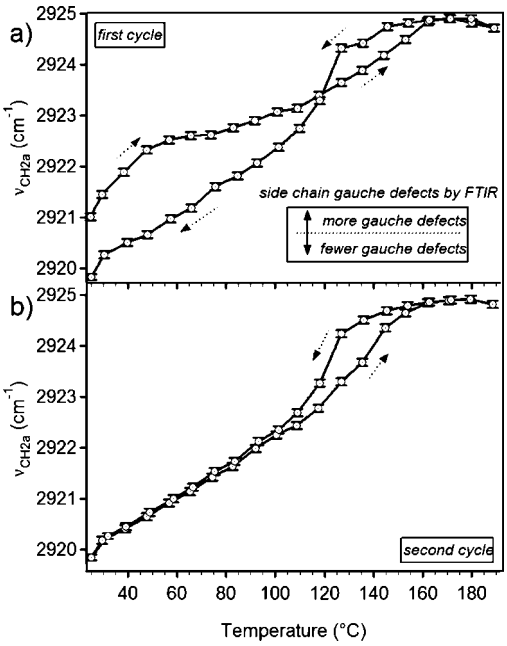

Figure 5. Response of pBTTT side-chain conformation to heating. FTIR methylene antisymmetric stretch position for the (a) first heating cycle and (b) second heating cycle. Raw FTIR data are provided in the Supporting Information. Experimental standard uncertainty of peak position is smaller than symbols.

maintained. The architecture of the mesophase provides a template for layer packing upon recrystallization.

While the XRD measurement explains at what temperature the pBTTT layer order develops, it does not reveal the molecular origin of the mesophase transition. To isolate conformational changes in the side chains and backbone, we apply polarized photon absorption spectroscopies, also with in situ heating. We first study changes in the side-chain conformation and orientation over a heating/cooling cycle.

The most important aspect of side chain conformation is the extent of gauche defects, which determines whether the chains are linear or coiled/random and qualitatively describes chain crystallinity. The extent of gauche defects can be qualitatively monitored by the energy of the antisymmetric methylene stretch, ν_{CH2a}, in IR spectroscopy. The ν_{CH2a} can vary from $\approx$2928 cm^{-1} for a liquidlike alkane to $\approx$2918 cm^{-1} for a fully crystalline alkane.[18,19] The evolution of the ν_{CH2a} over a heating cycle is shown in Figure 5a. The chains are initially quite well ordered. The chains exhibit a significant increase in the extent of gauche defects at T_{H1}, indicating that the melting of the metastable state is associated with alkane chain melting. The extent of side-chain disorder then increases monotonically, exhibits a significant increase near T_{H2}, and then reaches a plateau at $\approx$160 °C where the side chains are essentially liquidlike. Upon cooling, the side chains remain liquidlike until $\approx T_C$, where the chains appear to recrystallize. Below T_C, defects are gradually eliminated, and when annealing is complete, the chains are more ordered than they were initially, with $\nu_{CH2a} \approx 2919.5$ cm^{-1}.

The behavior of the side chain conformation during a second heating cycle, shown in Figure 5b, further confirms that the metastable state only occurs in films that have not been previously heated above T_{H2}. No inflection of ν_{CH2a} is observed near T_{H1} in the second heating cycle. Instead, ν_{CH2a} first increases monotonically, exhibits an inflection near T_{2H}, and then reaches a plateau at $\approx$160 °C where the side chains are liquidlike. When returning to room temperature, ν_{CH2a} significantly decreases at $\approx T_{1C}$.

IR spectroscopy reveals that the origin of the mesophase transition in pBTTT thin films is side-chain melting. The side chains must melt significantly before the layers can reorganize. This requirement is consistent with the significant level of side-chain interdigitation in the crystalline phase, both before and after annealing.[11] Crystalline and interdigitated side chains can be regarded as rigid links extending vertically that constrain the lateral motions of backbones and packed backbone layers. Only when the side chains are completely melted can the backbones freely move. At that point layer order defects can be removed and the quality of layer ordering dramatically improves (see Figure 3a). Upon cooling, the side chains recrystallize to capture and maintain the high level of layer order/alignment achieved in the mesophase. Side-chain interdigitation therefore provides a general mechanism to achieve and then preserve layer order because it both allows "repairs" to defective or small crystals that form during solidification from solution and then "locks in" the order.

Given that side-chain melting is the origin of the pBTTT mesophase transition, it follows that the metastable state of pBTTT may arise from an alternative side-chain packing arrangement. This packing arrangement apparently has a substantially lower melting temperature ($T_{H1} \approx 60$ °C) than the interdigitated, lowest free energy side-chain packing arrangement ($T_{H2} \approx 145$ °C). Importantly, no observable amount of the metastable state is formed after recrystallization through T_C. It is possible that formation of the metastable state requires that pBTTT pass through a solvent-induced (lyotropic) liquid crystal phase on solidification from solution or that pBTTT have a differently packed or less ordered backbone.

It is important to identify whether the dramatic film restructuring upon side-chain melting is accompanied by changes in the backbone conformation because it is within the backbone layers that charge carriers are formed and transport occurs. Ultraviolet−visible spectroscopic ellipsometry (SE) can simultaneously measure changes in the absorbance spectrum and backbone long-axis orientation.[19,20] The SE measurement provides the complex dielectric function $\epsilon = \epsilon' + i\epsilon''$ from 350 to 800 nm, which is assumed to be uniaxial with distinct components within the film plane and normal to it. The imaginary component $\epsilon''(\lambda)$ scales with pBTTT absorbance, which is dominated by its first singlet $\pi \rightarrow \pi^*$ transition. Changes in the peak energy of this transition (λ_{max}) with temperature, called thermochromism, provide insight into the torsional order of the backbone rings because λ_{max} systematically varies with conjugation length. Long conjugation lengths lead to higher values of λ_{max} (bathochromic or red shifts) while decreases in conjugation length lead to lower values of λ_{max} (hypsochromic or blue shifts). The $\pi \rightarrow \pi^*$ singlet transition

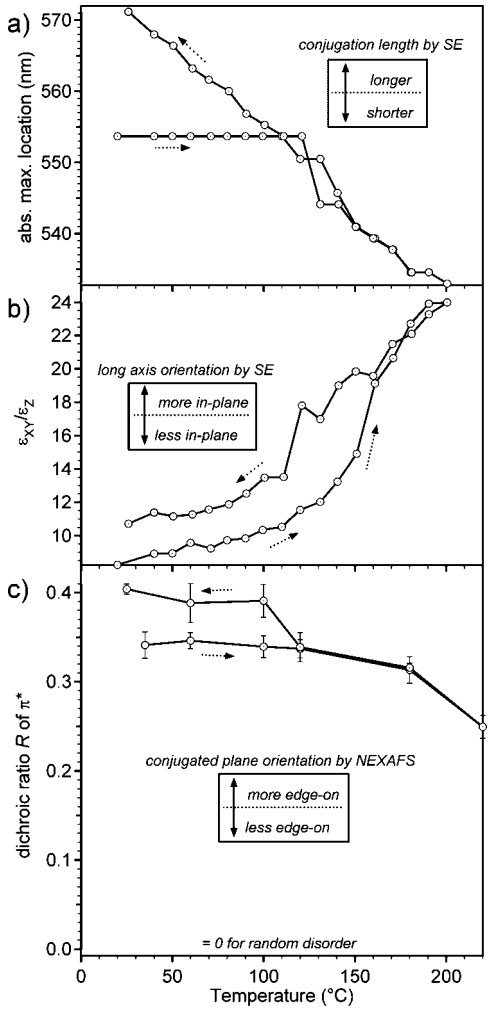

Figure 6. Response of pBTTT conjugated backbone to heating: (a) position of the absorption maximum in SE (thermochromism); (b) long axis orientation based on biaxial model fit to imaginary part of dielectric constant; (c) NEXAFS π^* dichroic ratio R, which indicates the average tilt of the conjugated planes of the pBTTT backbone. Raw SE and NEXAFS data are provided in the Supporting Information.

dipole moment lies along the pBTTT backbone, and the changing in-plane (ϵ_{xy}'') to out-of-plane (ϵ_z'') contributions to ϵ'' arise from the net backbone orientation with respect to surface normal.

The thermochromism of pBTTT is shown in Figure 6a. Initially, λ_{max} is 534 nm, and it remains approximately constant until ≈120 °C, when it begins to trend toward shorter wavelengths. No abrupt increase in torsional disorder is observed at T_{H1} or T_{H2}; the λ_{max} instead continues a gradual hypsochromic shift. Similarly, upon cooling, λ_{max} exhibits a gradual bathochromic shift, although we do observe a small jump in λ_{max} near T_C. The final λ_{max} is at a longer wavelength than it was initially, reflecting a longer backbone conjugation length that is consistent with the improved layer order measured by XRD. Upon a second heating (not shown), λ_{max} essentially retraces the cooling curve. This second-pass behavior suggests that the temperature-independent absorbance during first cycle heating is associated with competition between thermally activated ring torsion and the elimination of the metastable state, which modestly improves layer order. The generally monotonic shift in absorption, and the lack of transitions or inflection points, is consistent with a single structure for the backbone over the relevant temperature range. This is further supported by the lack of an isosbestic point in the dielectric spectra, similar to the thermochromism of regioregular P3AT's below their melting transitions.[21] The lack of backbone transitions is also consistent with the GIXD result that $\pi-\pi$ stacking persists in the mesophase above T_{H2}.

The average backbone long-axis orientation is indicated by the ratio of ϵ_{xy}'' to ϵ_z''. A film with perfect lamellar order would exhibit no ϵ_z''. The temperature dependence of this ratio is shown in Figure 6b. The backbone orientation modestly improves to 150 °C, where it increases abruptly toward greater orientation at T_{H2}. The backbone orientation appears to reach a plateau within the mesophase. Upon cooling, much of the in-plane backbone orientation achieved in the mesophase is lost. The greatest reductions in backbone orientation are observed near 120 °C. The final backbone orientation is more in-plane than it was initially, but not as much as it was in the mesophase. In general, the backbone orientation trend follows the trend in overall layer order determined by specular XRD, which is reasonable because the in-plane character of individual backbones should be closely correlated to the planar alignment of the packed backbone layers. A measurable extent of backbone orientation is lost upon the recrystallization of the side chains, and we note that some peak intensity is also lost in the last stages of cooling in specular XRD. These losses suggest that the side-chain interdigitation in the crystal phase is not completely compatible with the structure of the mesophase, resulting in slight crystallization-induced strain and the formation of defects.

A final important aspect of backbone conformation is the orientation of the conjugated planes. The conjugated planes of pBTTT and other thiophene polymers typically adopt an edge-on orientation that allows π overlap in the film plane, although the planes prefer to tilt 20°−30° from a perfect edge-on arrangement.[10,22] The carbon−carbon 1s → π^* transition in near-edge X-ray absorption fine structure (NEXAFS) spectroscopy[23] can be used to follow the conjugated plane tilt over a heating cycle, with results shown in Figure 6c. The conjugated plane orientation is quantified by a dichroic ratio, R, which is positive with a maximum of 0.7 for "edge on" conjugated planes and negative with a maximum of −1.0 for plane-on or flat conjugated planes. $R = 0$ indicates a tilt of the conjugated plane normal near the magic angle of 54.7° or random tilt. The partial electron yield method employed is intrinsically surface sensitive, sampling approximately the top 6 nm of the film. We assume that the orientation is similar at the top and bottom of the film, as we previously showed for annealed pBTTT films using a delamination technique.[10] The conjugated plane dichroic ratio R decreases gradually at temperatures above ≈130 °C, indicating either greater tilt or increased disorder about the mean tilt. This decrease is consistent with the onset of the hypsochromic absorbance shift. No abrupt change of conjugated plane orientation is observed at T_{H1} or T_{H2}, and significant edge-on orientation is maintained through the mesophase transition and beyond. Upon cooling, the preferred edge-on orientation is gradually restored, with a small step coincident with T_C, and the final conjugated plane orientation is more edge-on than it was initially. The conjugated plane orientation trend exhibits some similarity to the thermochromism trend, consistent with the assumption that thermally activated ring torsion causes the decrease in conjugation length and alters absorbance. The maintenance of a reasonably high level of edge-on conjugated plane orientation in the mesophase is consistent with the maintenance of π-stacking in the mesophase observed by GIXD.

This combination of measurements allows us to draw a detailed picture of the pBTTT mesophase above T_{H2}. It consists of highly ordered layers of π-stacked backbones separated by melted side chains. This phase may be classified as a high order smectic liquid crystal; it has layers lacking vertical registry that have aromatic subdomains within them with two-dimensional

spatial order and a preferred surface-relative tilt. We cannot explicitly exclude the possibility that T_{H2} is a crystal−crystal transition as recently proposed for thiophene oligomers;[24] however, it seems unlikely that vertical registry would be maintained by the disordered side chains. The melted side chains presumably afford sufficient molecular diffusivity to allow layer order and vertical domain size to improve dramatically. However, the mesophase must be quite viscous, as we do not observe film dewetting (atop OTS8) upon exceeding T_{2H}, but we do see it upon exceeding the phase transition temperature near 233 °C. Atomic force microscopy indicates that the lateral size of domains is greatly increased after annealing, confirming the high-viscosity yet liquidlike rheology of the mesophase.[10]

The structure of the pBTTT mesophase invites comparisons to the liquid-crystalline mesophases of other so-called "hairy rod" polymers with rigid backbones and alkane side-chain substitution. No structure or classification has yet been proposed for the few reports of well-defined mesophases in "hairy rods" with thiophene backbones.[7,25] We note that early thermal cycle studies of P3HTs synthesized without regioregular control suggest the existence of a poorly defined, nematic-like disordered state at temperatures exceeding 100 °C, formed by the cooperative thermal disordering of side chains and backbones.[26,27] In contrast, the liquid crystalline properties of the polyfluorenes (PFs, both pure and copolymerized with thiophene) have been widely studied. Grell et al. first reported that PFs with branched side chains can exhibit a well-defined nematic mesophase and further demonstrated that heating films to this mesophase caused the PF backbones to adopt in-plane alignment on rubbed polyimide surfaces.[28] The alignment of PF backbones has been used to study anisotropy in carrier mobility[29] and electroluminescence.[30] Backbone alignment has also been used as a valuable tool to study the packing details of PFs. When PF backbones do exhibit regular spatial order, they typically assume a hexagonal structure in what is called an α-phase, which lacks regular π-stacking between backbones.[31,32] Other types of "hairy rods", with aromatic amide or ester backbones and linear side chains, can form smectic-like layered structures. These structures were termed "sanidic" by Ringsdorf in recognition of the "boardlike" behavior of the backbones,[33,34] which in these phases adopt a preferential conjugated plane orientation with respect to the smectic-like layering direction. The mesophase of pBTTT above T_{H2} very closely resembles this classification because it exhibits well-defined layers that have π-stacking order and preferential conjugated plane orientation within. The technological role of the high-order smectic pBTTT mesophase is distinct from that of the PF nematic state because it allows the formation of laterally large, well-ordered domains with excellent alignment with respect to the surface normal, leading directly to the high carrier mobility that can be achieved with this class of polymer semiconductors.

Heating to the mesophase improves the carrier mobility of pBTTT (and other polymer semiconductors that exhibit a mesophase[35]), by a factor of 2−5. It is possible to follow the change in carrier mobility through a heating cycle. The interpretation of this data is complicated, as is convolves at least four distinct processes: intrinsic thermally activated transport in the channel; intrinsic thermally activated injection at the contacts; thermal induced morphology changes in the channel; and thermal induced morphology changes at the contacts. A complete separation of these effects is beyond this paper. Nonetheless, we report the carrier mobility of pBTTT transistors throughout a thermal cycle in Table 1. The mobility increases gradually and monotonically through the T_{H1} transition. Above T_{H2}, the mobility decreases somewhat but remains of a similar magnitude, consistent with the maintenance of $\pi-\pi$ stacking observed in GIXD, the high levels of layer order/alignment in specular XRD, the in-plane backbone orientation from SE, and the edge-on conjugated plane orientation from NEXAFS. Upon cooling, mobility gradually increases, with the most rapid gains near T_C suggesting that the influence of the improved microstructure outweigh thermal activation in this region. The carrier mobility at 80 °C increases to a maximum factor of ≈4 over the as-cast mobility.

Table 1. Saturation Mobility of pBTTT TFTs over a First Heating Cycle[a]

temperature (°C)		mobility (cm^2/(V s))
25	as-cast, room temperature	0.11
100	above T_{H1}	0.30
180	above T_{H2}	0.22
80	below T_C	0.40
25	annealed, room temperature	0.37

[a] Data are extracted from transfer curves where $V_{DS} = -100$ V, transistor $L = 20$ μm, and $W = 10$ mm. Raw transfer curves are provided in the Supporting Information. Standard uncertainty of mobility is ±5%.

Conclusions

These measurements reveal that the molecular origin of the mesophase transition in high-performance semiconducting polymers is the melting of interdigitated and crystalline alkane side chains. Heating above this transition reaches a liquid-crystalline state with improved levels of layer order, $\pi-\pi$ stacking, backbone orientation, and excellent carrier mobility. Reinterdigitation of the chains upon cooling preserves the high level of order. Further advances in polymer semiconductor synthesis must consider the interplay among (1) the backbone/side chain interactions driving lamellar order, (2) side chain crystallinity and interdigitation (influenced by areal attachment density[11] and possibly attachment point) that provide a mechanism for three-dimensional crystallization, and (3) the mesophase and its liquidlike yet ordered structure that permits lateral domain growth. Careful synthetic design may soon result in new polymer semiconductors with even higher carrier mobilities and further improved processability.

Acknowledgment. Portions of this research were carried out at the Stanford Synchrotron Radiation Laboratory, a national user facility operated by Stanford University on behalf of the U.S. Department of Energy, Office of Basic Energy Sciences. R.J.K. and A.J.M. gratefully acknowledge support from the NIST/NRC postdoctoral fellowship program. D.M.D. thanks Prof. D.-Y. Yoon for useful discussions concerning classification. The authors thank Merck Chemicals for providing the polymer semiconductor.

Supporting Information Available: Specular XRD patterns, FTIR spectra, NEXAFS spectra, SE model fits, and OFET transfer curves. This material is available free of charge via the Internet at http://pubs.acs.org.

References and Notes

(1) Sirringhaus, H.; Kawase, T.; Friend, R. H.; Shimoda, T.; Inbasekaran, M.; Wu, W.; Woo, E. P. *Science* **2000**, *290*, 2123–2126.
(2) *Printed Organic and Molecular Electronics*; Gamota, D. R., Brazis, P., Kalyanasundaram, K., Zhang, J., Eds.; Kluwer Academic Publishers: New York, 2004.
(3) Hugger, S.; Thomann, R.; Heinzel, T.; Thurn-Albrecht, T. *Colloid Polym. Sci.* **2004**, *282*, 932–938.
(4) Street, R. A.; Northrup, J. E.; Salleo, A. *Phys. Rev. B* **2005**, *71*, 165202.
(5) Gundlach, D. J.; Lin, Y. Y.; Jackson, T. N.; Nelson, S. F.; Schlom, D. G. *IEEE Electron Device Lett.* **1997**, *18*, 87–89.
(6) Ong, B.; Wu, Y. L.; Jiang, L.; Liu, P.; Murti, K. *Synth. Met.* **2004**, *142*, 49–52.
(7) McCulloch, I.; Heeney, M.; Bailey, C.; Genevicius, K.; Macdonald, I.; Shkunov, M.; Sparrowe, D.; Tierney, S.; Wagner, R.; Zhang, W. M.; Chabinyc, M. L.; Kline, R. J.; McGehee, M. D.; Toney, M. F. *Nat. Mater.* **2006**, *5*, 328–333.

(8) Chabinyc, M. L.; Toney, M. F.; Kline, R. J.; McCulloch, I.; Heeney, M. *J. Am. Chem. Soc.* **2007**, *129*, 3226–3237.
(9) Sirringhaus, H.; Brown, P. J.; Friend, R. H.; Nielsen, M. M.; Bechgaard, K.; Langeveld-Voss, B. M. W.; Spiering, A. J. H.; Janssen, R. A. J.; Meijer, E. W.; Herwig, P.; de Leeuw, D. M. *Nature (London)* **1999**, *401*, 685–688.
(10) DeLongchamp, D. M.; Kline, R. J.; Lin, E. K.; Fischer, D. A.; Richter, L. J.; Lucas, L. A.; Heeney, M.; McCulloch, I.; Northrup, J. E. *Adv. Mater.* **2007**, *19*, 833-837.
(11) Kline, R. J.; DeLongchamp, D. M.; Fischer, D. A.; Lin, E. K.; Richter, L. J.; Chabinyc, M. L.; Toney, M. F.; Heeney, M.; McCulloch, I. *Macromolecules* **2007**, *40*, 7960-7965.
(12) Scherrer, P. *Nachr. Göttinger Gesell.* **1918**, 98.
(13) Prosa, T. J.; Moulton, J.; Heeger, A. J.; Winokur, M. J. *Macromolecules* **1999**, *32*, 4000–4009.
(14) Cho, S.; Lee, K.; Yuen, J.; Wang, G. M.; Moses, D.; Heeger, A. J.; Surin, M.; Lazzaroni, R. *J. Appl. Phys.* **2006**, 100.
(15) Zen, A.; Pflaum, J.; Hirschmann, S.; Zhuang, W.; Jaiser, F.; Asawapirom, U.; Rabe, J. P.; Scherf, U.; Neher, D. *Adv. Funct. Mater.* **2004**, *14*, 757–764.
(16) Kline, R. J.; McGehee, M. D.; Kadnikova, E. N.; Liu, J. S.; Frechet, J. M. J.; Toney, M. F. *Macromolecules* **2005**, *38*, 3312–3319.
(17) Kline, R. J.; McGehee, M. D.; Toney, M. F. *Nat. Mater.* **2006**, *5*, 222–228.
(18) Macphail, R. A.; Strauss, H. L.; Snyder, R. G.; Elliger, C. A. *J. Phys. Chem.* **1984**, *88*, 334–341.
(19) Gurau, M. C.; Delongchamp, D. M.; Vogel, B. M.; Lin, E. K.; Fischer, D. A.; Sambasivan, S.; Richter, L. J. *Langmuir* **2007**, *23*, 834–842.
(20) McBranch, D.; Campbell, I. H.; Smith, D. L.; Ferraris, J. P. *Appl. Phys. Lett.* **1995**, *66*, 1175–1177.
(21) Yang, C.; Orfino, F. P.; Holdcroft, S. *Macromolecules* **1996**, *29*, 6510–6517.
(22) Northrup, J. E. *Phys. Rev. B* **2007**, *76*, 245202.
(23) Stöhr, J. *NEXAFS Spectroscopy*; Springer-Verlag: Berlin, 1992; Vol. *392*.
(24) Curtis, M. D.; Nanos, J. I.; Moon, H.; Jahng, W. S. *J. Am. Chem. Soc.* **2007**, *129*, 15072–15084.
(25) Wu, Y. O.; Liu, P.; Ong, B. S.; Srikumar, T.; Zhao, N.; Botton, G.; Zhu, S. P. *Appl. Phys. Lett.* **2005**, 86.
(26) Winokur, M. J.; Spiegel, D.; Kim, Y.; Hotta, S.; Heeger, A. J. *Synth. Met.* **1989**, *28*, C419−C426.
(27) Tashiro, K.; Ono, K.; Minagawa, Y.; Kobayashi, K.; Kawai, T.; Yoshino, K. *Synth. Met.* **1991**, *41*, 571–574.
(28) Grell, M.; Bradley, D. D. C.; Inbasekaran, M.; Woo, E. P. *Adv. Mater.* **1997**, *9*, 798–802.
(29) Sirringhaus, H.; Wilson, R. J.; Friend, R. H.; Inbasekaran, M.; Wu, W.; Woo, E. P.; Grell, M.; Bradley, D. D. C. *Appl. Phys. Lett.* **2000**, *77*, 406–408.
(30) Grell, M.; Knoll, W.; Lupo, D.; Meisel, A.; Miteva, T.; Neher, D.; Nothofer, H. G.; Scherf, U.; Yasuda, A. *Adv. Mater.* **1999**, *11*, 671–675.
(31) Knaapila, M.; Lyons, B. P.; Hase, T. P. A.; Pearson, C.; Petty, M. C.; Bouchenoire, L.; Thompson, P.; Serimaa, R.; Torkkeli, M.; Monkman, A. P. *Adv. Funct. Mater.* **2005**, *15*, 1517–1522.
(32) Lieser, G.; Oda, M.; Miteva, T.; Meisel, A.; Nothofer, H. G.; Scherf, U.; Neher, D. *Macromolecules* **2000**, *33*, 4490–4495.
(33) Voigtmartin, I. G.; Simon, P.; Bauer, S.; Ringsdorf, H. *Macromolecules* **1995**, *28*, 236–242.
(34) Endres, B. W.; Ebert, M.; Wendorff, J. H.; Reck, B.; Ringsdorf, H. *Liq. Cryst.* **1990**, *7*, 217–239.
(35) Salleo, A.; Chen, T. W.; Volkel, A. R.; Wu, Y.; Liu, P.; Ong, B. S.; Street, R. A. *Phys. Rev. B* **2004**, *70*, 10.
(36) Certain equipment, instruments or materials are identified in this paper in order to adequately specify the experimental details. Such identification does not imply recommendation by the National Institute of Standards and Technology nor does it imply the materials are necessarily the best available for the purpose.

MA800440F